Progressive delamination of laminated composites via 1D models

Original
Progressive delamination of laminated composites via 1D models / Kaleel, I., Carrera, E., Petrolo, M.. - In: COMPOSITE STRUCTURES. - ISSN 0263-8223. - STAMPA. - 235:(2020). [10.1016/j.compstruct.2019.111799]

Publisher:
Elsevier

Published
DOI:10.1016/j.compstruct.2019.111799

Progressive delamination of laminated composites via 1D models

I. Kaleel*[1], E. Carrera†[1], and M. Petrolo‡[1]

[1]MUL^2 Group, Department of Mechanical and Aerospace Engineering,
Politecnico di Torino, Turin, Italy

Submitted to
Composite Structures

Author for correspondence:
Erasmo Carrera, Professor
MUL^2 Group, Department of Mechanical and Aerospace Engineering,
Politecnico di Torino,
Corso Duca degli Abruzzi 24,
10129 Torino, Italy,
tel: +39 011 090 6836,
fax: +39 011 090 6899,
e-mail: erasmo.carrera@polito.it

---

*Research Assistant, ibrahim.kaleel@polito.it
†Professor of Aerospace Structures and Aeroelasticity, erasmo.carrera@polito.it
‡Assistant Professor, marco.petrolo@polito.it

Abstract

This paper presents a novel numerical framework to simulate the progressive delamination in laminated structures based on 1D component-wise models. The proposed numerical tool is a part of the virtual testing platform built within the Carrera Unified Formulation, a hierarchical, higher-order structural framework to generate theories of structures via a variable kinematic approach. Formulated within the Lagrange polynomial CUF models, the component-wise approach models the components of a complex structure through 1D CUF models at reduced computational costs and 3D-like accuracies. The effectiveness of CUF-CW models to capture accurate 3D transverse fields are of interest to solve delamination problems by integrating a class of higher-order cohesive elements to simulate the cohesive mechanics among the various components of the structure. The present framework adopts a bilinear constitutive law based on the mixed-mode delamination propagation and an efficient arc-length solver based on an energy-dissipation constraint. The numerical results aim to verify the accuracy and computational efficiency of CUF-CW models through benchmark composite delamination problems including multiple delamination fronts and comparisons with reference literature solutions and standard 3D FEM models. The outcomes show multi-fold improvements in the analysis times, good matches with experimental results, and promising enhancements of the meshing process due to the absence of aspect ratio constraints.

Keywords: Delamination, FEM, Carrera Unified Formulation, Laminated composites, higher-order models

1 Introduction

The delamination is one of the most dominant forms of failure in laminated composites. It often arises due to events leading to barely visible damages, such as run-way debris impact or tool-drop during maintenance [1, 2]. Also, high inter-laminar stresses lead to through-the-thickness failures triggered by high localized effects due to geometric - e.g., stiffener terminations, free-edges - or material discontinuities - such as ply drop-off [1]. Since delamination can result in significant alterations of the load-bearing capacity of composite structures, especially under compression, understanding and predicting the onset and propagation of delamination events is crucial.

Within the finite element method (FEM), cohesive zone based models are common tools for the interface modeling in composites. Originally conceived by Dugdale [3] and Barenblatt [4], the cohesive fracture concept assumes the existence of a zone around a crack tip which separates the undamaged and delaminated zones of the interface. Hillerborg et al. first introduced the concept of cohesive zone modeling within FEM by developing a traction-separation law for estimating the strengths of unreinforced concrete beams [5]. Since then, several contributions addressing the cohesive zone modeling technique have followed including applications for ductile metals [6], bio-mechanics [7] and mixed-mode delamination in composites [8, 9, 10, 11]. The Virtual Crack Closure Technique (VCCT) is another approach based on the linear elastic fracture mechanics often introduced within FEM [12] requiring a predefined initial crack [13].

A precise delamination analysis involves the accurate resolution of the transverse stress field. Nowadays, the standard approach exploits computationally intensive three-dimensional (3D) or layer-wise two-dimensional (2D) FE models, thereby limiting their applicability at early design stages and simple geometries. Also, cohesive-based FE analyses have some shortcomings including the requirement of extremely refined meshes near the cohesive zone and convergence issues, specifically along the descending branch of the equilibrium path. Turon et al. proposed a set of engineering solutions to overcome some of the issues of the cohesive modeling within standard FEM, including a closed-form expression for the penalty stiffness estimation and cohesive strength based on the mesh density [14]. Such a formulation is scalable for large-scale progressive delamination problems. Xie and Waas proposed a discrete cohesive zone model (DCZM) to model delamination effectively [11]. DCZM uses rod elements to enforce the cohesive law, unlike the traditional continuum cohesive elements. FE within the scheme of the isogeometric analysis using B-splines and NURBS can model delamination [15, 16, 17]. Nguyen and coworkers demonstrated the effectiveness and robustness of higher-order FEM built within the isogeometric framework for various 2D and 3D delamination problems [15, 16]. In recent years, several authors have contributed towards the development of 1D FE coupled with refined zig-zag theory (RZT) for problems accounting for the delamination onset and propagation [18, 19]. Eijo et al. presented a numerical tool based on RZT to simulate the mode II delamination in laminated beams. Groh and Tessler introduced a class of computationally efficient beam models using a mixed form of RZT to capture the displacement and stress fields for composite laminates around embedded delaminations [19]. A 2D FE formulation for multi-layered beams under mixed-mode delamination problem is in Škec et al. [20].

Some of the attempts related to convergence issues include the introduction of a viscous regularization technique [21] and development of new classes of arc-length based solvers catering to the needs of fracture problems [22, 23]. Alfano and Crisfield introduced a new class of local arc-length methods in combination with a line search technique to significantly improve the robustness and efficiency of FE delamination solutions [22]. A numerically efficient solver based on the LaTIn domain decomposition method is of Allix et al. for problems involving multiple simultaneous delaminations [24]. A dissipation-based arc-length scheme by Gutiérrez is a tool for the robust simulation of fracture, in which the arc-length constraint uses the total energy-release rate [23]. Since the dissipated energy is a global quantity, no a priori selection of the zone or degree of freedom (DOF) is necessary, and the scheme provides stable convergence behaviors [25]. Such a scheme proved its validity for delamination and multiscale analyses of heterogeneous structures [15, 26].

The aim of this is to use a new class of higher-order 1D structural models for the progressive delamination analysis of laminated composites. The interface modeling capabilities stem from the Carrera Unified Formulation (CUF), a hierarchical formulation that provides a structured basis for generating different classes of structural theories by varying the kinematic definitions [27]. The component-wise (CW) approach [28] efficiently models the cohesive kinematics and simulate the interface behavior. The ability of CUF-CW models to accurately describe in-plane and transverse stress fields is the tool to model the onset and propagation of delaminations together with a bilinear mixed-mode cohesive constitutive model. The current work is an extension to the applications of CUF models for a class of nonlinear problems including bucking and post-buckling analyses [29], physically nonlinear models for metals and composites [30, 31], and micromechanical progressive failure analysis in composites [32].

The remainder of the paper is organized as follows: Section 2 elaborates on the 1D cohesive formulation within CUF. The section also discusses details of the mixed-mode cohesive constitutive law and dissipation-based arc length implementations. Numerical results are presented in Section 3 and conclusions are drawn in Section 4.

2 1D cohesive formulation

1D CUF models provide theories of structures via cross-sectional expansion functions $F_\tau(x,z)$ [27],

$$\mathbf{u} = \mathbf{u}_\tau(y) F_\tau(x,z), \quad \tau = 1, ..., M \tag{1}$$

where M is the number of terms in the expansion function. The choice of the expansion and its order does not affect the governing equations of the formulation. For instance, various classes of expansion functions are implementable, such as Taylor, Lagrange and Legendre polynomials, and trigonometric or exponential functions, but no formal modifications of the equations are necessary. This works adopted Lagrange polynomials, henceforth referred to as LE models, leading to a purely displacement-based higher-order model. Based on the original work by Carrera and Petrolo on LE models [28], the present paper exploits the modeling approach referred to as the CW to model various components of the problem.

2.1 Cohesive kinematics

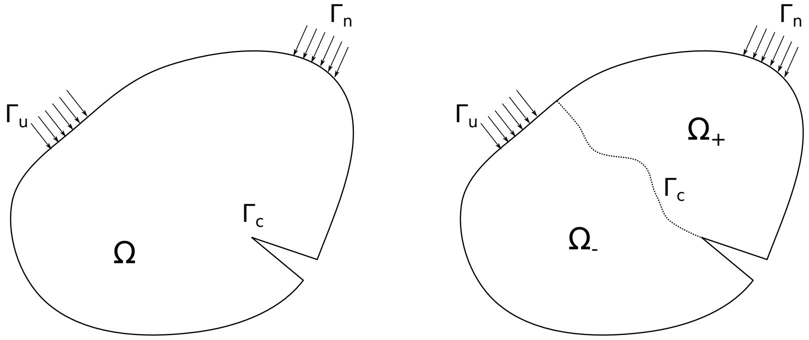

Figure 1: Description of the cohesive formulation

Let us consider a solid domain Ω bounded by Γ and containing a cracked zone Γ_c, as shown in Fig. 1. The essential boundary conditions act along the boundary Γ_u and prescribed tractions t_i act along Γ_n. The domain Ω has two domains, Ω_+ and Ω_-, along the crack boundary Γ_c, as depicted in Fig. 1. The governing equilibrium equations for the quasi-static problem are

$$\begin{aligned}
&\sigma_{ij,j} + b_i = 0 \quad in \;\; \Omega \qquad (2)\\
&u_i = \bar{u} \quad in \;\; \Gamma_u, \qquad \sigma_{ij} n_j = t_i \quad in \;\; \Gamma_n\\
&\sigma_{ij} n_j^+ = \tau_i^+ = -\tau_i^- = -\sigma_{ij} n_j^- n_j^- \quad in\, \Gamma_c
\end{aligned}$$

where σ_{ij} is the Cauchy stress field within the domain due to the external loading t_i with normals to the boundary Ω_n denoted by n_i. b_i are the body forces, $\bar{u}$ are the prescribed displacements along the Dirichlet boundary Γ_u and τ_i^+, τ_i^- are the closing tractions acting along the crack domain Γ_c. Via the the Principle of Virtual Displacements (PVD) and accounting for the additional contributions due to the cohesive crack,

$$\begin{gathered}
\delta L_{int} + \delta L_{coh} - \delta L_{ext} = 0 \qquad (3)\\
\delta L_{int} = \int_\Omega \delta \boldsymbol{\epsilon} : \boldsymbol{\sigma}\, dV\\
\delta L_{coh} = \int_{\Gamma_c} \delta[[\mathbf{u}]] \cdot \boldsymbol{\tau} d\Gamma_c\\
\delta L_{ext} = \int_\Omega \delta \mathbf{u} \cdot \mathbf{b} d\Omega + \int_{\Gamma_n} \delta \mathbf{u} \cdot \mathbf{t}\, d\Gamma_n
\end{gathered}$$

where δ indicates the virtual variation, L_{int}, L_{coh} and L_{ext} refer to the bulk strain energy, work due to the cohesive crack and the external loading, respectively, and $[[\mathbf{u}]]$ denotes the displacement jump across the cohesive surface. The kinematics of the interface stems from the displacement jump across the interface boundary [33],

$$[[u_i]] = u_i^+ - u_i^- \tag{4}$$

where u_i^+ and u_i^- denote the displacements in direction i on the upper (Ω_+) and lower surface (Ω_-) of the interface. As depicted in Fig. 2, a six-node cohesive Lagrange cross-section elements is introduced with expansion function expressed as:

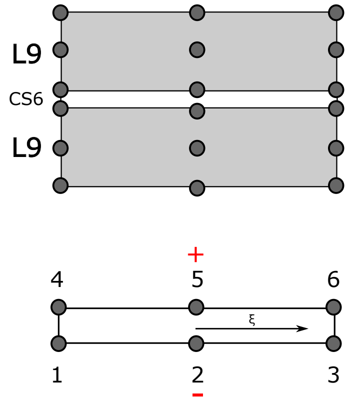

Figure 2: Six-node cohesive Lagrange cross-section elements (CS6)

$$\begin{array}{ll} \mathbf{u}^+ = F_1\mathbf{u}_4 + F_2\mathbf{u}_5 + F_3\mathbf{u}_6 & \left.\begin{array}{l} F_1 = \frac{1}{2}\xi(1-\xi) \\[2ex] F_2 = -(1-\xi)(1+\xi) \\[2ex] F_3 = \frac{1}{2}\xi(1+\xi) \end{array}\right\} \begin{array}{l} \xi_1 = -1 \\[2ex] \xi_2 = 0 \\[2ex] \xi_3 = 1 \end{array} \\ \mathbf{u}^- = F_1\mathbf{u}_1 + F_2\mathbf{u}_2 + F_3\mathbf{u}_3 & \end{array} \tag{5}$$

2.2 Cohesive constitutive modeling

This work adopted the mixed-mode cohesive constitutive modeling of Camanho and his coworkers [10, 34]. Formulated within the scheme of damage mechanics, the cohesive constitutive law relates the cohesive traction t_j to the displacement jump Δ_j in the local coordinate system as follows:

$$t_j = (1-d)D^0_{ij}\Delta_j - dD^0_{ij}\delta_{3j} < -\Delta_3 > \tag{6}$$

where d is the damage variable, $< \cdot >$ the MacAuley bracket and D^0_{ij} the initial stiffness tensor defined as a function of the penalty parameter K and Kronecker delta δ_{ij},

$$D^0_{ij} = \delta_{ij} K \tag{7}$$

The second term in Eq. 6 prevents non-physical post-decohesion interfacial penetrations. The damage variable d makes use of a damage criterion built within the equivalent displacement jump space,

$$F(\lambda^t, r^t) = G(\lambda^t) - G(r^t) \leq 0 \quad \forall \quad t \geq 0 \tag{8}$$

where t denotes the quasi-static time and r^t is the damage threshold for the current time. Based on the mixed-mode bilinear constitutive formulation, G is

$$G(\lambda) = \frac{\Delta^f(\lambda - \Delta^0)}{\lambda(\Delta^f - \Delta^0)} \tag{9}$$

$$d^t = G(r^t) \qquad \forall \quad r^t = \max_s \left\{ r^0, \lambda \right\} \quad 0 \geq s \geq t \tag{10}$$

where Δ^0 and Δ^f are the equivalent displacements at the damage onset and complete failure (d=1) respectively, which are functions of mode I (G$_{Ic}$) and mode II (G$_{IIc}$) fracture toughness, mode mixity and an experimentally obtained parameter η. λ is the current equivalent non-negative displacement jump. As depicted in Fig. 3, the propagation criteria stems the formulation by Benzggagh and Kenane [35],

$$G_c = G^c_I + (G^c_{II} - G^c_I)\left(\frac{G^c_I}{G_T}\right)^\eta, \quad G_T = \frac{G_{II}}{G_I + G_{II}} \tag{11}$$

The displacement jump criterion is

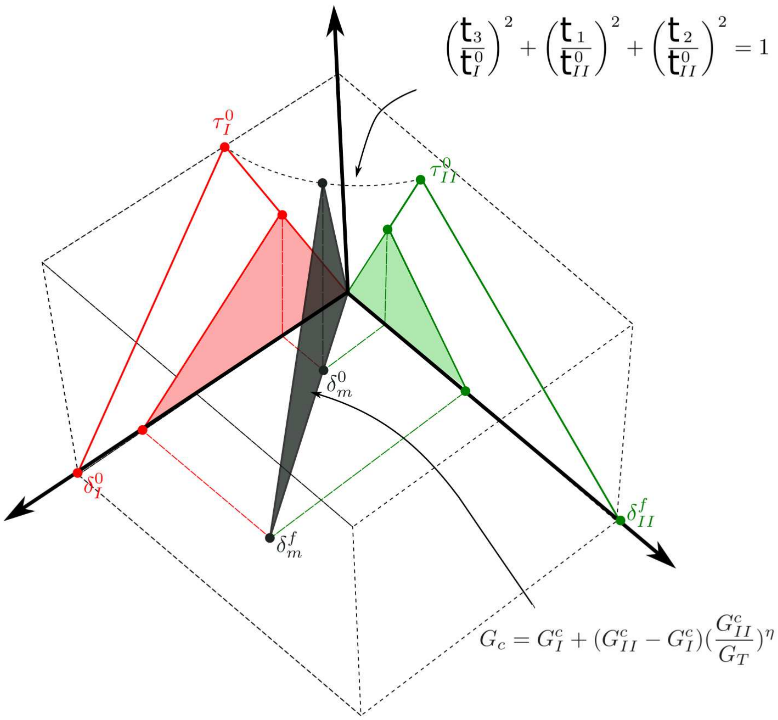

Figure 3: Bilinear mixed-mode cohesive criteria [35]

$$\Delta^0 = \sqrt{\Delta_3^2 + (\Delta_{shear}^2 - \Delta_3^2)B^\eta} \tag{12}$$

$$B = \frac{G_{shear}}{G_T}, \qquad \Delta_{shear} = \sqrt{\Delta_I^2 + \Delta_{II}^2}, \qquad G_{shear} = G_I + G_{II} \tag{13}$$

The tangent constitutive matrix derives by the differentiation of the traction-displacement relation in Eq. 6 [34],

$$\begin{aligned} \dot{t} &= D_{ij}^{tan}\dot{\Delta}_j \\ D_{ij}^{tan} &= \begin{cases} \left\{D_{ij} - K\left[1 + \delta_{3j}\frac{<-\Delta_j>}{\Delta_j}\right]\left[1 + \delta_{3j}\frac{<-\Delta_i>}{\Delta_i}\right]H\Delta_i\Delta_j, \quad r < \lambda < \Delta^f\right\} \\ D_{ij}, \quad r > \lambda \ or \ \Delta^f < \lambda \end{cases} \end{aligned} \tag{14}$$

where H is the scalar parameter defined as

$$H = \frac{\Delta^f\Delta^0}{(\Delta^f - \Delta^0)\lambda^3} \tag{15}$$

2.3 Finite Element Formulation

The 3D displacement vector reads

$$\mathbf{u}(x, y, z) = \{u_x \, u_y \, u_z\}^T \tag{16}$$

The stress and strain states are

$$\boldsymbol{\epsilon} = \{\epsilon_{xx} \, \epsilon_{yy} \, \epsilon_{zz} \, \epsilon_{yz} \, \epsilon_{xz} \, \epsilon_{xy}\}^T \qquad \boldsymbol{\sigma} = \{\sigma_{xx} \, \sigma_{yy} \, \sigma_{zz} \, \sigma_{yz} \, \sigma_{xz} \, \sigma_{xy}\}^T \tag{17}$$

With small strain assumptions, the linear strain-displacement relations and stress-strain law are

$$\boldsymbol{\epsilon} = \mathbf{b}\mathbf{u}, \qquad \mathbf{b}^T = \begin{bmatrix} \partial_x & 0 & 0 & 0 & \partial_z & \partial_z \\ 0 & \partial_y & 0 & \partial_z & 0 & \partial_x \\ 0 & 0 & \partial_z & \partial_y & \partial_x & 0 \end{bmatrix}; \qquad \boldsymbol{\sigma} = \mathbf{C}\,\boldsymbol{\epsilon} \tag{18}$$

where $\mathbf{b}$ is the differential operator and $\mathbf{C}$ is the material matrix. By employing standard FE shape functions, the generalized displacement field is

$$\mathbf{u}\,(x, y, z) = N_i(y)\,F_\tau(x, z)\,\mathbf{u}_{\tau i}(y) \quad \forall \quad \tau = 1, 2, \dots, M \quad i = 1, 2, \dots p + 1 \tag{19}$$

$$\mathbf{u}_{\tau i} = [u_{x_{\tau i}} \, u_{y_{\tau i}} \, u_{z_{\tau i}}] \tag{20}$$

where N_i is the beam shape function of order p and $\mathbf{u}_{\tau i}$ is the nodal displacement vector. The choice of the shape function order p and the order of the expansion function terms M remain independent and are input of the analysis. Similarly, the displacement field on the upper and lower face of the CS element is

$$\mathbf{u}^+ = F_\tau N_i \mathbf{u}^+_{\tau i} \qquad \mathbf{u}^- = F_\tau N_i \mathbf{u}^-_{\tau i} \qquad [[\mathbf{u}]] = F_\tau N_i \left(\mathbf{u}^+_{\tau i} - \mathbf{u}^-_{\tau i}\right) \tag{21}$$

where $\mathbf{u}^+$ and $\mathbf{u}^-$ are the displacements along the upper and lower edges of the CS element, respectively. Therefore, the equilibrium equations (Eq. 3) in terms of FE matrices become

$$\mathbf{k}^{bulk}_{ij\tau s}\mathbf{u}_{\tau i} + \mathbf{k}^{coh}_{ij\tau s}[[\mathbf{u}_{\tau i}]] - \mathbf{p}_{\tau i} = 0 \tag{22}$$

where $\mathbf{k}^{bulk}_{ij\tau s}$ and $\mathbf{k}^{bulk}_{ij\tau s}$ refer to the Fundamental Nuclei (FN) of the bulk and cohesive stiffness matrix, respectively, and the FN for the external loading is $\mathbf{p}_{\tau i}$. For the sake of conciseness, readers may use the book by Carerra et al. for detailed information on the derivation and implementation of FNs for the bulk stiffness matrix and external loading [27]. Based on Eq. 3, FN of cohesive forces are

$$f^{+}_{coh_{\tau i}} = \int_{\Gamma_c} F_\tau N_i \, \mathbf{u}^{+}_{\tau i} \, t^{+} d\Gamma_c \quad f^{-}_{coh_{\tau i}} = \int_{\Gamma_c} F_\tau N_i \, \mathbf{u}^{-}_{\tau i} \, t^{-} d\Gamma_c \tag{23}$$

To formulate the fundamental nuclei of the cohesive tangent matrix, the rate form of the cohesive constitutive law is (Eq. 14)

$$\dot{\mathbf{t}}^c = \mathbf{Q}\,\mathbf{D}^{tan}\,\mathbf{Q}^T[[\dot{\mathbf{u}}]] = \mathbf{Q}\,\mathbf{D}^{tan}\,\mathbf{Q}^T \;\; F_\tau N_i \,(\mathbf{u}^{+}_{\tau i} - \mathbf{u}^{-}_{\tau i}) \tag{24}$$

where $\mathbf{Q}$ is the orthogonal transformation matrix used for the transformation between the local and global system for cohesive elements. FN for the cohesive tangent matrix stems from the linearizion of the cohesive force vector (Eq. 23),

$$k^{coh}_{ij\tau s} = \int_{\Gamma_c} F_\tau N_i \mathbf{Q}\,\mathbf{D}^{tan}\,\mathbf{Q}^T F_s N_j d\Gamma_c \tag{25}$$

The integration of cohesive elements via the standard Gauss quadrature leads to responses with spurious oscillations, especially when large stress gradients are present across a cohesive element [36]. The present work made use of the Newton-Cotes integration scheme for integrating the FN tangent stiffness matrix and internal force vector. The discrete equation in weak form is

$$\mathbf{f}^{int} + \mathbf{f}^{coh} - \mathbf{f}^{ext} = 0 \tag{26}$$

where $\mathbf{f}^{int}$, $\mathbf{f}^{coh}$ and $\mathbf{f}^{ext}$ denote the global vectors for internal, cohesive and external forces, respectively.

Based on the works of Gutiérrez, this paper adopted an arc-length solver with a path-following constraint based on the energy release rate [23, 25]. Therefore, the global system of equation reads

$$\begin{bmatrix} \mathbf{f}^{int}(\mathbf{u}) - \lambda \mathbf{f}^{ext} \\ g(\mathbf{u}, \lambda) \end{bmatrix} = 0 \tag{27}$$

where $\mathbf{f}^{int}(\mathbf{u})$ includes contributions from bulk as well cohesive finite elements and g is the energy-release constraint equation expressed as

$$g = \frac{1}{2}\mathbf{f}_{ext}^{T}(\lambda_0 \Delta\mathbf{u} - \Delta\lambda \mathbf{u}_0) - \Delta\tau \tag{28}$$

where $\mathbf{f}_{ext}^{T}$ is the global unit external force vector, $\Delta\tau$ is the dissipation path parameter, λ_0 and $\mathbf{u}_0$ are the last converged load factor and displacement vector, respectively. The amount of energy dissipated during a given load increment is always a monotonically increasing quantity. To avoid numerical issues in non-dissipative regions - such as pure elastic loading - the implementation used a switching algorithm via threshold values. The algorithm switches to displacement/force controlled loading during non-dissipative regions and to dissipation-controlled according to the energy threshold. In addition, the path parameter, $\Delta\tau$, varies during the course of computation to limit the number of steps required to minimum without any cut-backs. Given the optimal value of iterations per increment k_{opt}, the path parameter for a given increment i is [23]

$$\Delta\tau^{i} = \Delta\tau^{i-1}\frac{k_{opt}}{k^{i-1}} \tag{29}$$

where k^{i-1} refers to the number of iterations required in the last converged load step.

3 Numerical results

This section presents three study cases, namely, the End Notch Flexure test (ENF) with a pure mode II delamination propagation, the mixed-mode bending test (MMB) with two mode-mix ratios, and a composite specimen with multiple delamination fronts. Unless otherwise specified, the results from 1D and 3D FE were obtained from in-house codes.

3.1 ENF test

This section aims to verify the accuracy and performance of the implemented cohesive model. The material is isotropic as in the analytical solution from [9], see Table 1. Figure 4 illustrates the geometry and boundary conditions of the specimen. Contact elements along the initial crack surface avoid the inter-penetration. The solution scheme made use of the energy-based arc-length method with an initial lambda λ_0 of 50 and a unit force applied as P. The final displacement, u_z is 3.5 mm. CUF models for this case have 4L9-2CS6 and 6L9-3CS6 cross-section discretizations, as shown in Fig. 5. 3D FEM models served as verification tools via standard linear brick elements, see Table 2 showing also DOF and the total analysis time for all models.

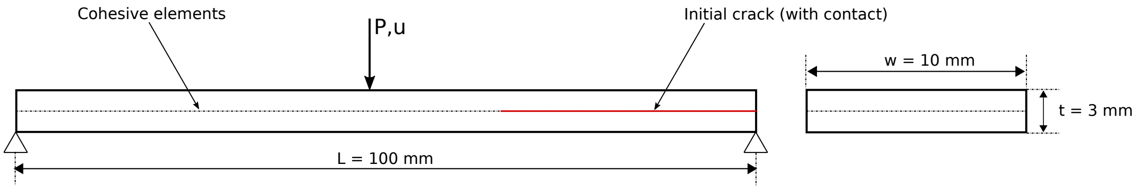

Figure 4: Geometry and loading for ENF

Table 1: Material properties for ENF

Bulk material		Cohesive material		
E	ν	τ_1	K	G_{IIC}
(GPa)	(-)	(MPa)	(Nmm^{-3})	Nmm^{-1}
150.0	0.25	80.0	10^6	1.45

Figure 6a depicts the comparison of equilibrium curves from 3D FEM models, 4L9-2CS6, and the analytical solution developed by Mi et al. [9]. The paths from Different CUF cross-section models

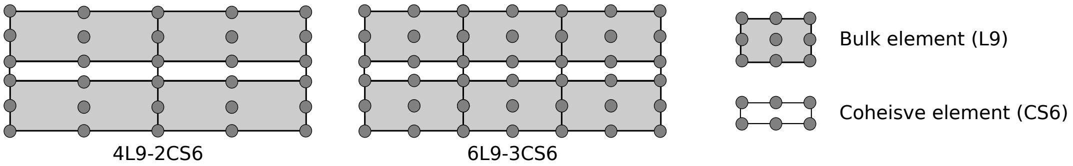

Figure 5: Cross-section meshes for ENF

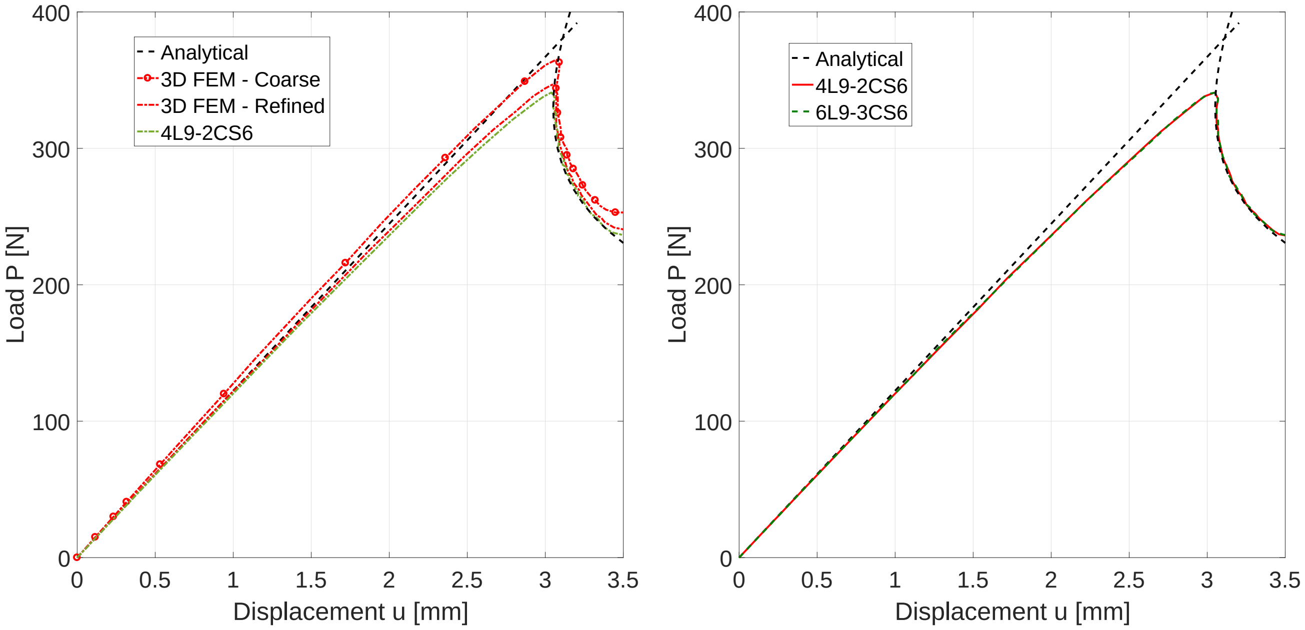

(a) (b)

Figure 6: ENF, comparison of equilibrium curves for (a) 4L9-2CS6 and 3D FEM models and (b) 4L9-2CS6 and 6L9-3CS6

Table 2: Model information for ENF specimen test

Model	Description	DOF	Analysis time (s)
4L9-2CS6	Cross-section has 4L9 bulk elements with 2 CS6 cohesive elements, see Fig. 5. The beam has 80 B4 elements.	21690	383
6L9-3CS6	Cross-section has 6L9 bulk elements, i.e., three per layer, with 3 CS6 cohesive elements, see Fig. 5. The beam has 80 B4 elements.	30366	666
3DFEM - Coarse	Linear brick elements with a mesh density of 4 × 240 × 4 and 4 × 240 cohesive elements.	21690	420
3DFEM - Refined	Linear brick elements with a mesh density of 4 × 360 × 4 and 4 × 360 cohesive elements.	32490	893

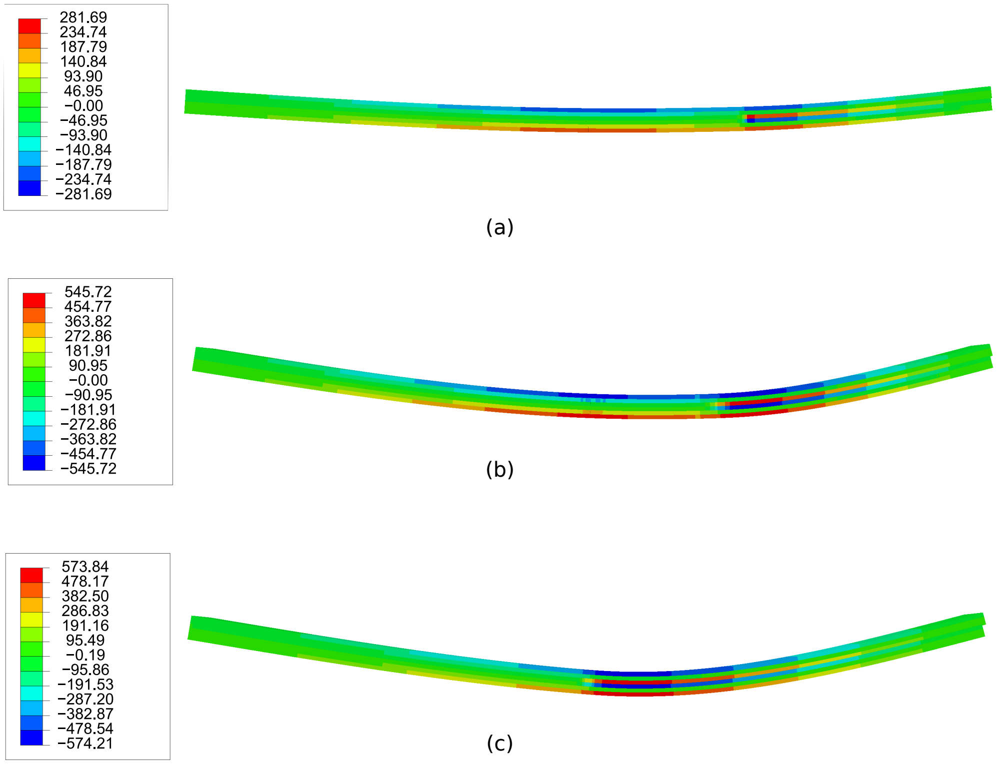

Figure 7: ENF, σ_{yy} (MPa) for 4L9-2CS6 model at various load values, (a) P = 30.08 N, (b) P = 228.4 N and (c) P = 280.3 N

are in Fig. 6b. The deformed configuration along with σ_{yy} are Fig. 7 for the 4L9-2CS6. The results suggest that

1. The comparison with the analytical solution proved the accuracy of the present 1D formulation.
2. The coarse and refined 1D models provide almost identical results matching the refined 3D. The coarse 3D, on the other hand, tends to overestimate the equilibrium curve.
3. The coarse 1D model and the refined 3D provide the same accuracy, but the former requires half the computational time. The absence of aspect ratio constraints in the 1D formulation permits to use coarser meshes than 3D and with higher-order expansions. Therefore, locally, the displacement and stress fields have higher resolutions than the 3D models.

3.2 MMB test

The MMB is a widely adopted standardized testing method (ASTM-D5528) for characterizing the mixed-mode fracture toughness in laminated composites for any mixed-mode ratio [37]. Different mode ratios stem by varying the loading arm length c with the Double Cantilever Beam test (DCB) and ENF as border cases. The present investigation exploited the experimental and numerical investigations of Camanho et al. [10] for verification purposes. Figure 8 depicts the geometry and boundary conditions. The material is a unidirectional AS4/PEEK carbon-reinforced composite with fibers oriented along the beam direction, see Table 3 for properties. The mode-mix ratios are 0.5 and 0.8. Table 4 enlists the geometric properties and applied loading conditions for each ratio. As in Table 5, the numerical results used two CUF models. Similar to the previous numerical case, contact elements avoided the inter-penetration of the initial crack surface. Based on the rigid body motion assumption for the loading arm, the load-point displacement u is [10, 38]:

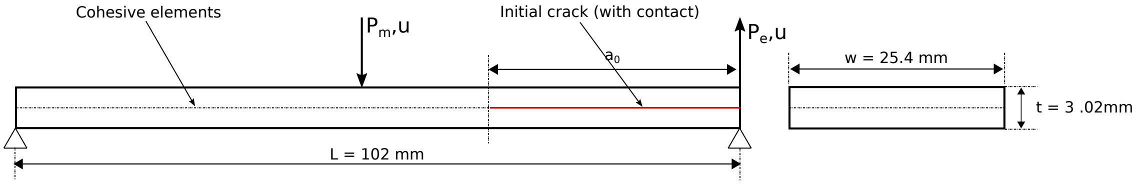

Figure 8: Geometry and loading for MMB

Table 3: Material properties for MMB

E_{11} (GPa)	E_{22}=E_{33} (GPa)	G_{12}=G_{13} (GPa)	G_{23} (GPa)	$\nu_{12} = \nu_{13}$ (-)	G_{IC} (Nmm^{-1})	G_{IIC} (Nmm^{-1})	τ_3 (MPa)	τ_2 (MPa)	K_0 (Nmm^{-3})
122.7	10.1	5.5	3.7	0.25	0.969	1.719	80	100	10^6

$$u = \frac{2c + L}{L} u_m - \frac{2c}{L} u_e \tag{30}$$

where u_m and u_e are the displacements obtained at the middle and end of the specimen, see Fig. 8. The energy-based arc length method was the solution scheme with an initial lambda λ_0 of 10 and 25 for mode-mix ratios of 0.5 and 0.8, respectively. The analysis ended at 6.5 mm and 6.1

mm. Balzani used 3D FE models mixed-mode delamination [38] whereas Camanho 2D ones [10]. Figure 9(a) compares equilibrium curves obtained using the 8L9-4CS6-60B4 model against experimental and numerical results. Convergence of equilibrium curves for different 1D models are in Fig. 9(b). Table 6 compares the maximum load obtained by 1D CUF and experimental and numerical reference models. The analysis times required for all the numerical models are in Table 7. The results suggest that

Table 4: Geometric properties and load values for different mode-mix ratio for MMB test [10, 38]

G_{II}/G_T	G_c (Nmm^{-1})	a_0 (mm)	c (mm)	P_m (N)	P_e (N)
0.5	1.131	34.1	44.4	1.87P	0.87P
0.8	1.376	31.4	28.4	1.56P	0.56P

Table 5: Model information for MMB test

Model	Description	DOF
8L9-4CS6-40B4	Cross-section has 8L9, 4 per each layer, and 4CS6 cohesive elements. The beam has 40B4 elements.	19602
8L9-4CS6-60B4	Cross-section has 8L9, 4 per each layer, with 4CS6 cohesive elements. The beam has 60B4 elements.	29322

Table 6: Comparison of maximum loads obtained using 8L9-4CS6-60B4 model for MMB against experimental and numerical models

G_{II}/G_T	Experimental [10]	Camanho et al. [10]		Balzani et al. [38]		CUF-CW	
		Value	Error	Value	Error	Value	Error
	(N)	(N)	(%)	(N)	(%)	(N)	(%)
0.5	275.35	236.6	14.1	251.2	8.8	261.0	5.2
0.8	518.66	479.9	7.5	438.3	15.5	494.5	4.7

1. 1D models detected the equilibrium curves with a good agreement if compared to experimental and numerical results from the literature.
2. The refinement of the 1D mesh led to marginal improvements of the solution.

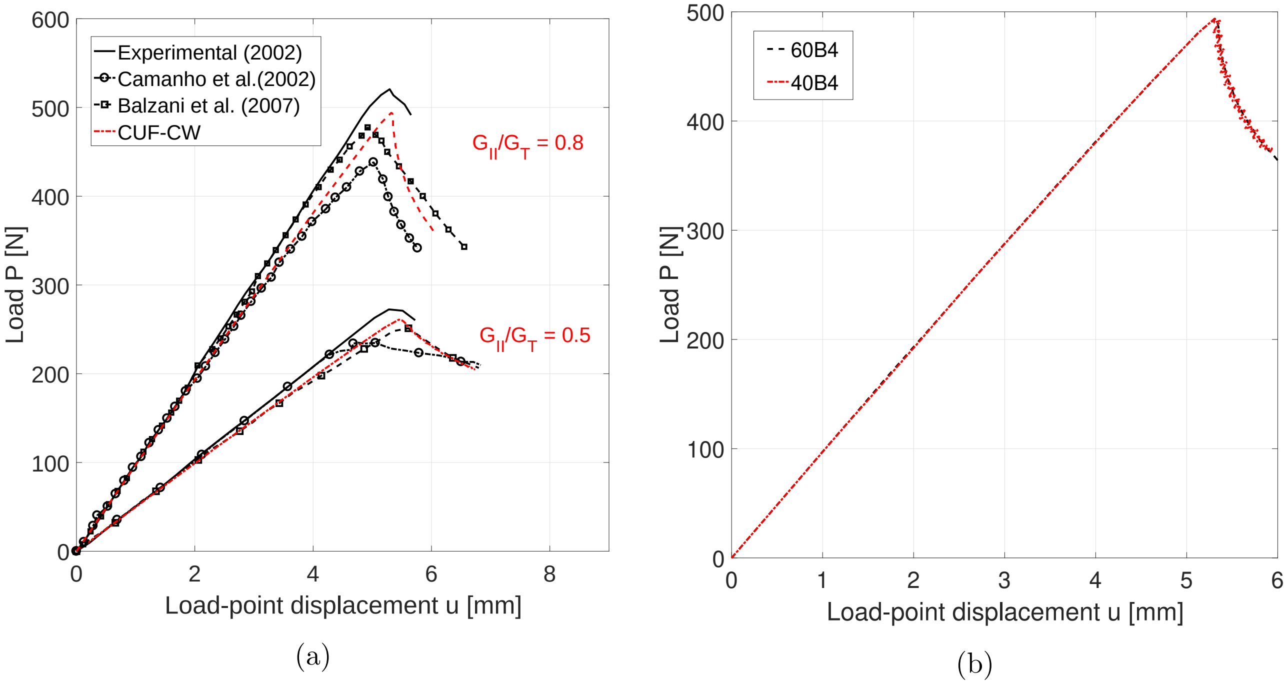

Figure 9: Equilibrium curves for mixed-mode bending test: (a) Results from 1D CUF using 8L9-4CS6-60B4 and experimental and numerical results from the literature and (b) convergence of 1D CUF models for the 0.8 mode-mix ratio

Table 7: Costs of the analyses for the MMB test

Model	Analysis time (hh:mm)
8L9-4CS6-40B4	0:27
8L9-4CS6-60B4	0:45

3. The present models improved the accuracy to experimental results concerning the peak load if compared to previous numerical models.

3.3 Multiple delaminations of composite specimens

Robinson et al. investigated multiple mixed-mode delaminations in a carbon-fiber laminate through numerical as well experimental studies [39]. As illustrated in Fig. 10, the problem consists of two initial cracks. The first crack is along the mid-plane on the left-end of the specimen and the second one is two plies below and right of the first initial crack. The problem is common in literature as it exhibits a complex equilibrium path and, therefore, serves as a benchmark [22, 15]. The material properties of the specimen are in Table 8. Figure 11 illustrates the modeling technique adopted using CUF approach. According to the position of the initial crack, the model has various cross-section configurations. The modeling approach preserves the node compatibility at the interfaces of different sets of beams indicated by the two-colored beam nodes in Fig. 11. Verifications used three additional models based on standard linear brick elements with linear 3D cohesive elements and varying mesh density as in Table 9. The energy-based arc-length method solved the numerical problem with an initial lambda λ_0 of 1 and a force applied as P, and a termination condition of Δ equal to 24 mm. Alfano and Crisfield performed the multiple delamination analysis us-

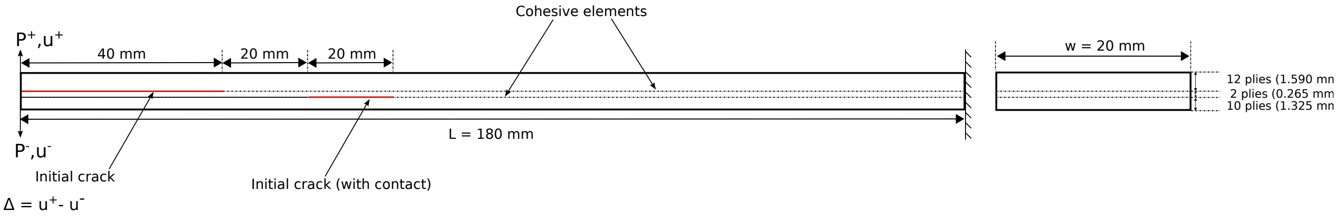

Figure 10: Geometry and boundary conditions for multiple delaminations

Table 8: Material properties for multiple delaminations [39, 15]

E_1 (GPa)	E_2=E_3 (GPa)	G_{12} (GPa)	ν_{12}=ν_{13} (-)	G_{IC} (Nmm^{-1})	G_{IIC} (Nmm^{-1})	τ_3 (MPa)	τ_1 (MPa)	K (Nmm^{-3})
115.0	8.5	4.5	0.29	0.33	0.8	8.0	3.3	2.5×10^5

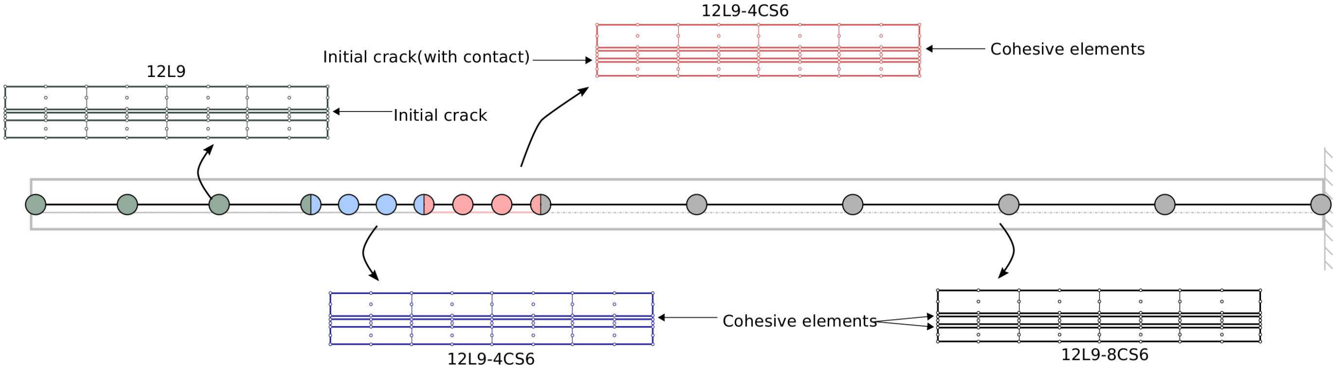

Figure 11: CUF models for multiple delaminations

Table 9: Model descriptions for multiple delaminations

Model	Description	DOF
12L9-4CS6	Cross-section has 12L9 elements with a combination of 4CS6/8CS6 cohesive elements inserted between the layers based on the position of cracks, see Fig. 11. The beam has 77B4 elements.	56376
3DFEM - Coarse	Linear brick elements with a mesh density of 8x230x6. The mesh density is equivalent to that of 12L9-4CS6 configuration, amounting to similar DOF	56133
3DFEM - Medium	Linear brick elements with a mesh density of 8x458x6 with twice the mesh density along the beam as compared to the 3DFEM - Coarse	111537
3DFEM - Refined	Linear brick elements with a mesh density of 8x619x6 with three times the mesh density along the beam as compared to the 3DFEM - Coarse	150660

ing 2D standard FEM elements equipped with local arc-length and a line-search based numerical solver [22]. Nguyen and Nguyen-Xuan developed a 2D higher-order Bèzier element along with an energy-based arc-length method and efficiently solved the multiple delamination analysis of composite specimens [15]. Figure 12a compares the equilibrium curves obtained using CUF with the experimental and numerical results available from the literature [15, 39, 22]. Equilibrium curves obtained from CUF and 3D FEM models with varying mesh density are in Fig. 12. Table 10 enlists the information pertaining the total analysis time of various models. Figure 13 depicts the equilibrium curve from CUF along with the deformation state at specific load instances. Contour plots for delaminated zones in the top and bottom surfaces of the specimen at various instances are in Fig. 14. The results suggest that

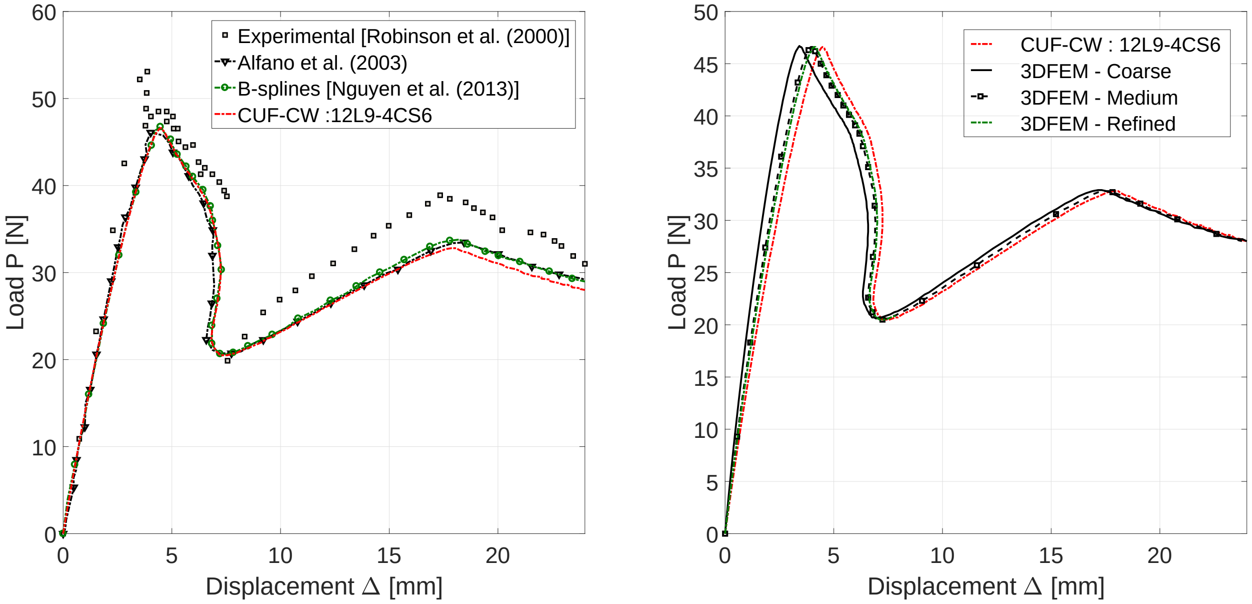

(a)

(b)

Figure 12: Equilibrium curves for multiple delaminations: (a) Comparison of CUF with experimental and literature results [39, 22, 15] and (b) comparison between CUF and 3D FEM with varying mesh density

1. As verified via reference solutions, CUF accurately captures the complex equilibrium curve for multiple delaminations.

2. The refining process of 3D models converges to CUF. In particular, although the size of the

Table 10: Analysis times for multiple delaminations

Model	Analysis Time (hh:mm)
12L9-4CS6	1:47
3DFEM- Coarse	1:25
3DFEM - Medium	4:44
3DFEM - Refined	7:15

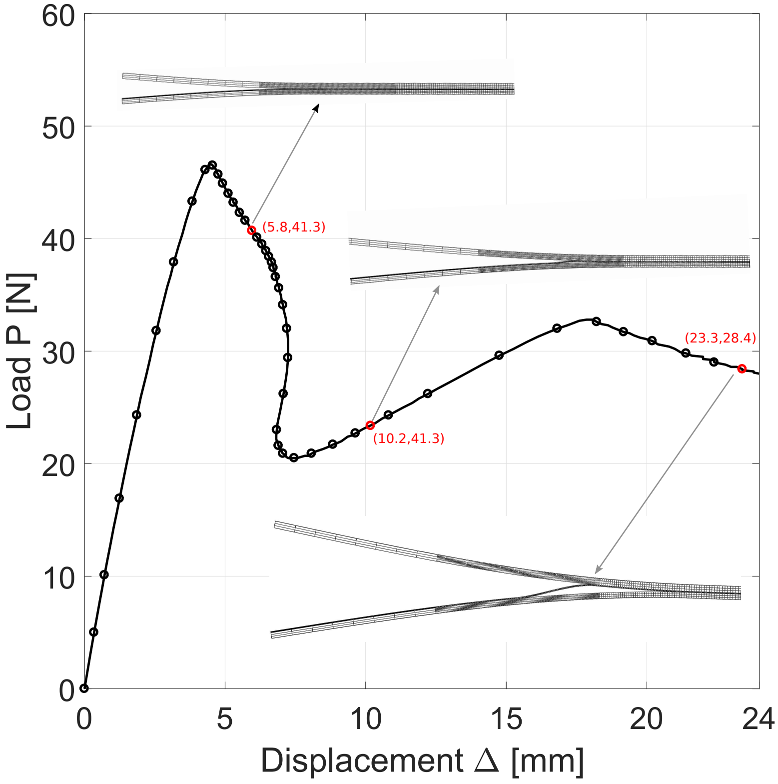

Figure 13: Equilibrium curves and deformed states via CUF for multiple delaminations

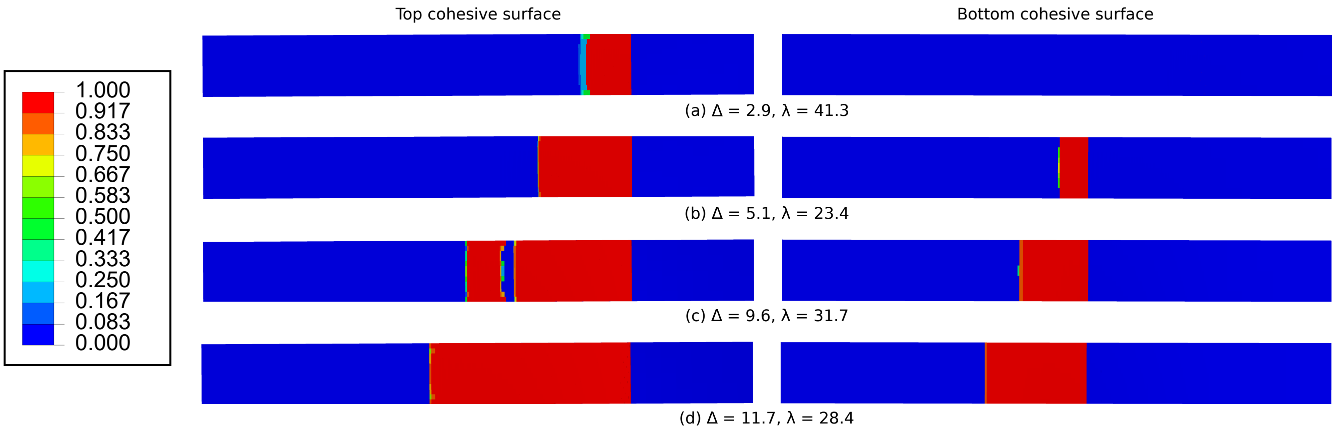

(a) Δ = 2.9, λ = 41.3

(b) Δ = 5.1, λ = 23.4

(c) Δ = 9.6, λ = 31.7

(d) Δ = 11.7, λ = 28.4

Figure 14: Contour plots of the delamination index - 0: intact, 1: fully delaminated - at the top and bottom cohesive surfaces via CUF for multiple delaminations

problem for 12L9-4CS6 and 3D FEM - Coarse configurations is similar, the 3D FEM - Coarse model presents visible differences in the equilibrium path.

3. CUF models have multi-fold better efficiency regarding the analysis times than standard 3D FEM.
4. The present formulation can capture the progressive delamination propagation along multiple fronts.
5. From a modeling standpoint, the CUF modeling improves the meshing process by assigning various cross-section configurations to individual beams whereas the discretization and insertion of cohesive elements within a 3D FEM model may lead to a cumbersome process due to the high number of FE elements.

4 Conclusion

The paper extends 1D higher-order FE models to the delamination modeling to increase the computational efficiency. Cohesive modeling capabilities make use of the CUF approach to exploit refined displacement field along the cross-section and obtain complete and accurate 3D stress and displacement fields. The approach makes use of the mixed-mode cohesive constitutive law and a global dissipation energy-based arc -length method, and verified via various numerical examples including the end-notch flexure test, mixed-mode bending test, and multiple delamination fronts. The analysis of the results suggest that

- CUF tends to outperform standard 3D FEM with multi-fold efficiency regarding the analysis times. Such an outcome stems from the lower amounts of DOF required by CUF models.
- The absence of aspect ratio constraints in 1D models permits to enrich the modeling capabilities only by adopting refined structural theories instead of re-meshing.
- In the MMB test, CUF models provided significant improvements concerning the prediction of peak loads if compared to other numerical tests and experimental results.

- The use of cohesive elements within CUF may lead to more efficiency in the modeling as the elements are cross-section features and non-homogeneous 1D elements and compatibilities are enforceable straightforwardly.

Future extensions include the implementation of more advanced delamination models and the application to delamination problems in large-scale structures such as a skin-stringer debonding simulation. Within the view of multi-fold efficiency, the present models may be of great advantage within concurrent multiscale frameworks.

5 Acknowledgments

This research work has been carried out within the project FULLCOMP (FULLy analysis, design, manufacturing, and health monitoring of COMPosite structures), funded by the European Union Horizon 2020 Research and Innovation program under the Marie Skłodowska-Curie grant agreement No. 642121.

References

[1] M. R. Wisnom. The role of delamination in failure of fibre-reinforced composites. *Philosophical Transactions of the Royal Society A: Mathematical, Physical and Engineering Sciences*, 370:1850–1870, 2012.

[2] S. Abrate. Modeling of impacts on composite structures. *Composite Structures*, 51(2):129 – 138, 2001.

[3] D. S. Dugdale. Yielding of steel sheets containing slits. *Journal of the Mechanics and Physics of Solids*, 8(2):100 – 104, 1960.

[4] G. I. Barenblatt. The mathematical theory of equilibrium cracks in brittle fracture. volume 7 of *Advances in Applied Mechanics*, pages 55 – 129. Elsevier, 1962.

[5] A. Hillerborg, M. Modéer, and P. E. Petersson. Analysis of crack formation and crack growth in concrete by means of fracture mechanics and finite elements. *Cement and Concrete Research*, 6(6):773 – 781, 1976.

[6] A. Needleman. A continuum model for void nucleation by inclusion debonding. *Journal of Applied Mechanics*, 54(3):525–531, 1987.

[7] J. P. Clech, L. M. Keer, and J. L. Lewis. A crack model of a bone cement interface. *Journal of Biomechanical Engineering*, 106(3):235—-243, 1983.

[8] O. Allix and P. Ladeveze. Interlaminar interface modelling for the prediction of delamination. *Composite Structures*, 22:235–242, 1992.

[9] Y. Mi, M. A. Crisfield, G. A. O. Davies, and H. B. Hellweg. Progressive delamination using interface elements. *Journal of Composite Materials*, 32(14):1246–1272, 1998.

[10] P. P. Camanho, C. G. Davila, and M. F. De Moura. Numerical simulation of mixed-mode progressive delamination in composite materials. *Journal of Composite Materials*, 37(16):1415–1438, 2003.

[11] D. Xie and A. M. Waas. Discrete cohesive zone model for mixed-mode fracture using finite element analysis. *Engineering Fracture Mechanics*, 73:1783–1796, 2006.

[12] E. F. Rybicki and M. F. Kanninen. A finite element calculation of stress intensity factors by a modified crack closure integral. *Engineering Fracture Mechanics*, 9(4):931 – 938, 1977.

[13] R. Krueger. Virtual crack closure technique: history, approach, and applications. *Applied Mechanics Reviews*, 57(2):109–143, 2004.

[14] A. Turon, C. G. Davila, P. P. Camanho, and J. Costa. An engineering solution for mesh size effects in the simulation of delamination using cohesive zone models. *Engineering fracture mechanics*, 74(10):1665–1682, 2007.

[15] V. P. Nguyen and H. Nguyen-Xuan. High-order B-splines based finite elements for delamination analysis of laminated composites. *Composite Structures*, 102:261–275, 2013.

[16] V. P. Nguyen, P. Kerfriden, and S. P. A. Bordas. Two-and three-dimensional isogeometric cohesive elements for composite delamination analysis. *Composites Part B: Engineering*, 60:193–212, 2014.

[17] S. Hosseini, J. J. C. Remmers, C. V. Verhoosel, and R. De Borst. Propagation of delamination in composite materials with isogeometric continuum shell elements. *International Journal for Numerical Methods in Engineering*, 102(3-4):159–179, 2015.

[18] A. Eijo, E. Oñate, and S. Oller. A numerical model of delamination in composite laminated beams using the LRZ beam element based on the refined zigzag theory. *Composite Structures*, 104:270–280, 2013.

[19] R. M. J. Groh and A. Tessler. Computationally efficient beam elements for accurate stresses in sandwich laminates and laminated composites with delaminations. *Computer Methods in Applied Mechanics and Engineering*, 320:369–395, 2017.

[20] L. Škec, G. Jelenić, and N. Lustig. Mixed-mode delamination in 2d layered beam finite elements. *International Journal for Numerical Methods in Engineering*, 104(8):767–788, 2015.

[21] Y. F. Gao and A. F. Bower. A simple technique for avoiding convergence problems in finite element simulations of crack nucleation and. *Modelling and Simulation in Materials Science and Engineering*, 12:453–463, 2004.

[22] G. Alfano and M. A. Crisfield. Solution strategies for the delamination analysis based on a combination of local-control arc-length and line searches. *International Journal for Numerical Methods in Engineering*, 58(7):999–1048, 2003.

[23] M. A. Gutiérrez. Energy release control for numerical simulations of failure in quasi-brittle solids. *Communications in Numerical Methods in Engineering*, 20:19–29, 2004.

[24] O. Allix, P. Kerfriden, and P. Gosselet. On the control of the load increments for a proper description of multiple delamination in a domain decomposition framework. *International Journal for Numerical Methods in Engineering*, 83(11):1518–1540, 2010.

[25] C. V. Verhoosel, J. J. C. Remmers, and M. A. Gutiérrez. A dissipation-based arc-length method for robust simulation of brittle and ductile failure. *International Journal for Numerical Methods in Engineering*, 77(9):1290–1321, 2009.

[26] V. P. Nguyen, O. Lloberas-Valls, M. Stroeven, and L. J. Sluys. Computational homogenization for multiscale crack modeling. implementational and computational aspects. *International Journal for Numerical Methods in Engineering*, 89(2):192–226, 2012.

[27] E. Carrera, M. Cinefra, E. Zappino, and M. Petrolo. *Finite element analysis of structures through unified formulation*. John Wiley and Sons, 2014.

[28] E. Carrera and M. Petrolo. Refined beam elements with only displacement variables and plate/shell capabilities. *Meccanica*, 47(3):537–556, 2012.

[29] A. Pagani and E. Carrera. Large-deflection and post-buckling analyses of laminated composite beams by Carrera Unified Formulation. *Composite Structures*, 170:40–52, 2017.

[30] E. Carrera, I. Kaleel, and M. Petrolo. Elastoplastic analysis of compact and thin-walled structures using classical and refined beam finite element models. *Mechanics of Advanced Materials and Structures*, In Press.

[31] I. Kaleel, M. Petrolo, and E. Carrera. Elastoplastic and progressive failure analysis of fiber-reinforced composites via an efficient nonlinear microscale model. *Aerotecnica Missili and Spazio*, 97(2):103–110, 2018.

[32] I. Kaleel, M. Petrolo, A. M. Waas, and E. Carrera. Micromechanical progressive failure analysis of fiber-reinforced composite using refined beam models. *Journal of Applied Mechanics*, 85(February):1–8, 2018.

[33] O. Allix and C. Alberto. Geometrical and interfacial non!linearities in the analysis of delamination in composites. *International Journal of Solids and Structures*, 36:2189–2216, 1999.

[34] A. Turon, P. P. Camanho, J. Costa, and C. G. Davila. A damage model for the simulation of delamination in advanced composites under variable-mode loading. *Mechanics of Materials*, 38:1072–1089, 2006.

[35] M. L. Benzeggagh and M. Kenane. Measurement of mixed-mode delamination fracture toughness of unidirectional glass / epoxy composites with mixed-mode bending apparatus. *Composite Science and Technology*, 56:439–449, 1996.

[36] J. C. J. Schellekens and R. de Borst. On the numerical integration of interface elements. *International Journal for Numerical Methods in Engineering*, 36(April 1992):43–66, 1993.

[37] ASTM D 5528-94a. Standard test method for mode i interlaminar fracture toughness of unidirectional fiber-reinforced polymer matrix composites. Technical report, ASTM, 1994.

[38] C. Balzani and W. Wagner. An interface element for the simulation of delamination in unidirectional fiber-reinforced composite laminates. *Engineering Fracture Mechanics*, 75:2597–2615, 2008.

[39] P. Robinson, T. Besant, and D. Hitchings. Delamination growth prediction using a finite element approach. *European Structural Integrity Society*, 27:135–147, 2000.